THE ASTROPHYSICAL JOURNAL, 567:1091–1101, 2002 March 10

X-RAY SPECTRAL AND TIMING OBSERVATIONS OF CYGNUS X-2

S. PIRAINO,[1,2] A. SANTANGELO,[2] AND P. KAARET[1]

Received 2001 July 23; accepted 2001 October 11

ABSTRACT

We report on a joint *BeppoSAX*/*RXTE* observation of the Z-type low-mass X-ray binary Cyg X-2. The source was in the so-called high overall intensity state and in less than 24 hr went through all three branches of the Z track. The continuum X-ray spectrum could be described by the absorbed sum of a soft thermal component, modeled as either a blackbody or a multicolor disk blackbody, and a Comptonized component. The timing power spectrum showed several components, including quasi-periodic oscillations in the range 28–50 Hz while the source was on the horizontal branch (horizontal branch oscillation; HBO). We found that the HBO frequency was well correlated with the parameters of the soft thermal component in the X-ray spectrum. We discuss implications of this correlation for models of the HBO.

Subject headings: accretion, accretion disks — stars: individual (Cygnus X-2) — stars: neutron — X-rays: binaries — X-rays: general — X-rays: stars

1. INTRODUCTION

Cygnus X-2 is a bright, persistent, low-mass X-ray binary (LMXB). It consists of a neutron star with an optically measured mass of $M_X > 1.78 \pm 0.23\ M_\odot$ (Orosz & Kuulkers 1999), orbiting the evolved, late-type companion V1341 Cyg, with a period of $\sim$9.8 days (Cowley, Crampton, & Hutchings 1979; Casares, Charles, & Kuulkers 1998). Although Cyg X-2 is one of longest-known and best-studied LMXBs, a clear understanding of its behavior has not yet been obtained.

Cyg X-2 is classified as a Z source because of its behavior when studied on an X-ray color-color diagram (CCD). Z sources follow a one-dimensional trajectory in the two-dimensional CCD, tracing out a Z shape as the source evolves between different spectral states. The parts of the Z are referred to as the horizontal branch (HB) at the top of the Z, the normal branch (NB) along the diagonal of the Z, and the flaring branch (FB) at the base of the Z. Z sources move continuously along the Z diagram, and the position of the source within the Z is believed, from simultaneous multiband (radio, UV, optical, and X-ray) observations (Hasinger et al. 1990), to be related to the mass accretion rate, with accretion at a minimum at the left end of the HB and at a maximum at the right end of the FB. However, the behavior of Z sources is not described by a single parameter because, on timescales of weeks to months, the morphology and position of the Z track in the CCD vary. Kuulkers, van der Klis, & Vaughan (1996) described the phenomenology for Cyg X-2 in terms of three overall intensity levels (high, medium, and low), with different morphology for the Z track in the different intensity levels.

Z sources, including Cyg X-2, show complex X-ray spectrum, requiring a superposition of several spectral components. Different composite models, including thermal bremsstrahlung together with blackbody radiation, two blackbodies, a power law plus thermal bremsstrahlung, a multitemperature blackbody disk plus boundary layer blackbody, and a Comptonized spectrum, have all been found to describe adequately the data. Unfortunately, spectral modeling alone has not led to unique identification of the physical origin of the various spectral components. Further observations relating the X-ray spectra to other source parameters are required.

Z sources also show rich X-ray timing power spectra including several components and varying with position in the CCD. Cyg X-2 shows quasi-periodic oscillations (QPOs), with frequency varying between $\sim$15 and $\sim$60 Hz, on the horizontal branch and on the upper part of the normal branch (HBOs), and high-frequency QPOs (kHz QPOs), ranging between 300 and 900 Hz have been detected on the HB (Wijnands et al. 1998). Slower QPOs, with frequencies of 5–7 Hz, are observed on the lower part of the normal branch (called NBOs). Sometimes HBOs are observed simultaneously with the NBOs, indicating that these QPOs should be produced by different mechanisms. Agreement is lacking on a unique model to explain the HBOs, the NBOs, or the kHz QPOs. Correlations between the timing parameters and other source parameters may help limit the number of viable models for the QPOs.

In this paper, we present joint timing and spectral observations of Cygnus X-1 obtained with *RXTE* and *BeppoSAX*. The goal of our observations was to obtain simultaneous X-ray spectral and timing data for Cyg X-2 in order to study correlations between the spectral and timing parameters. The observations and analysis are described in § 2. Results on the color and intensity evolution are presented in § 3, on timing power spectra in § 4, and on energy spectra in § 5. The correlations between spectral and timing properties are described in § 6. We discuss the implications of our results in § 7.

2. OBSERVATIONS AND ANALYSIS

On 2000 June 2–3, we performed a joint observation of Cyg X-2 with the *RXTE* and *BeppoSAX* satellites. The pointing was carried out between 2000 June 2 13:11 UT and June 3 17:23 UT with *RXTE* (Bradt, Rothschild, & Swank 1993) and between 2000 June 2 18:56 UT and June 3 14:25 UT with the *BeppoSAX* Narrow-Field Instruments (NFIs; Boella et al. 1997).

Spectral data obtained from the *RXTE* Proportional Counter Array (PCA) in 129 photon energy channels with a

[1] Harvard-Smithsonian Center for Astrophysics, 60 Garden Street, Cambridge, MA 02138; piraino@ifcai.pa.cnr.it, pkaaret@cfa.harvard.edu.
[2] Istituto di Fisica Cosmica con Applicazioni all'Informatica (IFCAI), Consiglio Nazionale delle Ricerche (CNR), via Ugo La Malfa 153, 90146 Palermo, Italy.

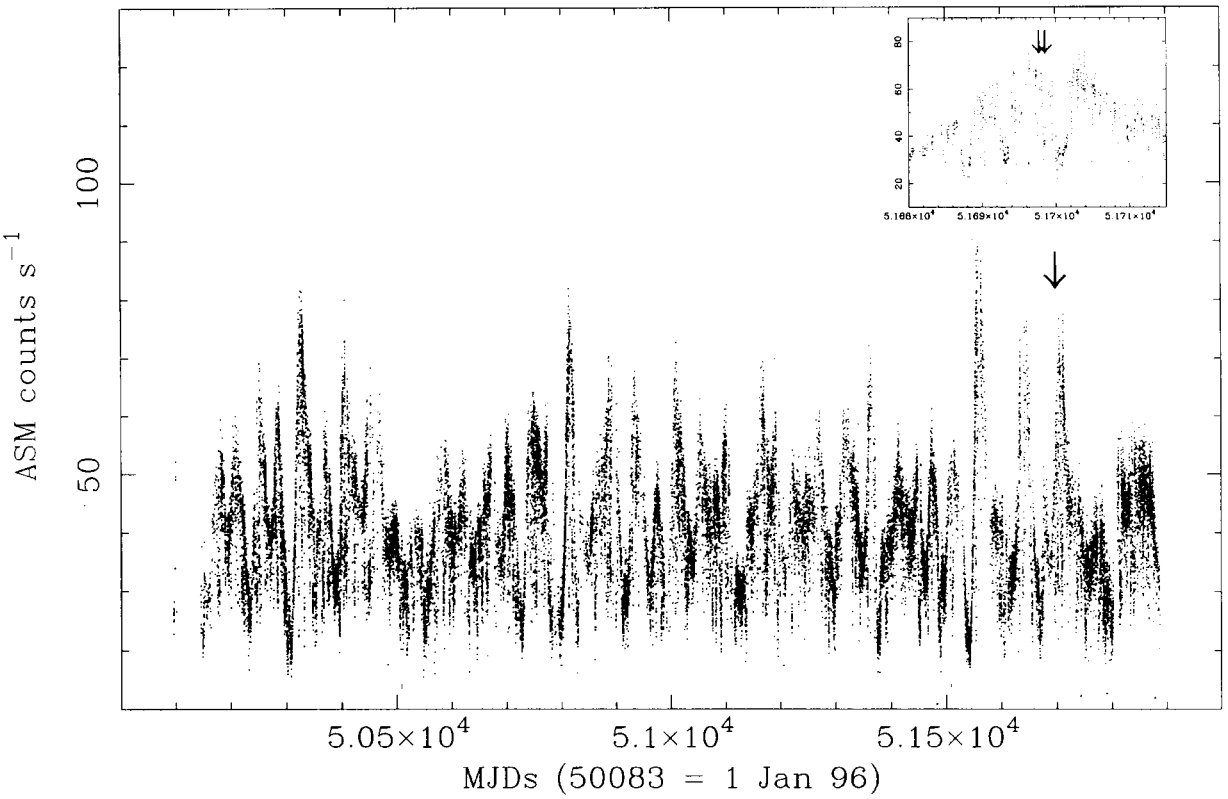

FIG. 1.—*RXTE* All Sky Monitor light curve (1.3–12.1 keV) of Cyg X-2 from 1996 January to 2000 December. Long-term X-ray variations are clearly visible. The *RXTE*/*BeppoSAX* observation is indicated with an arrow on the right. The inset shows the complex time variability of the source around the observation.

time resolution of 16 s (Standard 2) were used to extract a color-color diagram (CCD) and a hardness-intensity diagram (HID). The soft and hard colors were defined as count-rate ratios between 4.0–6.4 keV and 2.6–4.0 keV and between 9.7–16 keV and 6.4–9.7 keV. The intensity was defined as the PCU2 count rates in the energy band 2.6–16 keV. All count rates were background-subtracted. We used only PCU2 for the intensity and color analysis, because only it and PCU0 were on during all observations and because PCU0 suffered from a propane layer leak, which made the energy calibration very uncertain.

Timing data obtained from the PCA with a time resolution of 125 μs in single-bit (one energy channel) modes for the energy bands 2.0–5.8 keV, 5.8–10.1 keV, 10.1–21.4 keV, and 21.4–120 keV were used to obtain power spectra. We note that the data mode used does not allow us to remove events from PCU0. Thus, as a result of the propane layer leak, the true energy bands for PCU0 likely differ from these nominal ranges. However, our basic result on the energy dependence of the timing noise (that the noise features are stronger at higher energies) is not sensitive to the details of the energy band boundaries.

To search for fast kHz QPOs, we performed fast Fourier transforms on 2 s segments, added all power spectra obtained within each selected observation interval, and then searched for excess power in the 200–2048 Hz range. No kHz QPOs with a chance probability of occurrence of less than 1% were found, either in the full-band data or in the data above 5.8 keV. The kHz QPO previously found from Cyg X-2 occurred in the medium overall intensity state (Wijnands et al. 1998). No kHz QPOs have been observed during the high-intensity state.

To study the low-frequency behavior, we performed fast Fourier transforms on 64 s segments, and we added the 64 s power spectra obtained, once for all energy bands and once for the three highest-energy bands, within each continuous observation interval. The expected Poisson noise level due to counting statistics was estimated, taking into account the effects of the dead time, and subtracted from each power spectrum, and the power spectra were normalized to fractional rms. Each 0.1–100 Hz total power spectrum was fitted as described below.

Data from the *BeppoSAX* NFIs were used to extract broadband energy spectra. The NFIs are four co-aligned instruments covering the 0.1–200 keV energy range: LECS (0.1–10 keV), MECS (1.3–10 keV), HPGSPC (7–60 keV), and PDS (13–200 keV). The net on-source exposure times were 11, 27, 35, and 20 ks for LECS, MECS, HPGSPC, and PDS, respectively. LECS and MECS data were extracted in circular regions, centered on Cyg X-2's position, having radii of 8′ and 4′, respectively. The same circular regions in blank field data were used for the background subtraction. Cyg X-2 is sufficiently bright during this observation that the background subtraction does not affect the fit results. Spectra accumulated from dark Earth data and during off-source intervals were used for the background subtraction in the HPGSPC and PDS, respectively. The LECS and MECS spectra have been rebinned to sample the instrument resolution with the same number of channels at all energies. Logarithmic rebinning was used for the HPGSPC and PDS spectra.

We investigated the source power and energy spectrum in different regions of the HID. Energy spectra of each NFI were create over five different HID intervals where

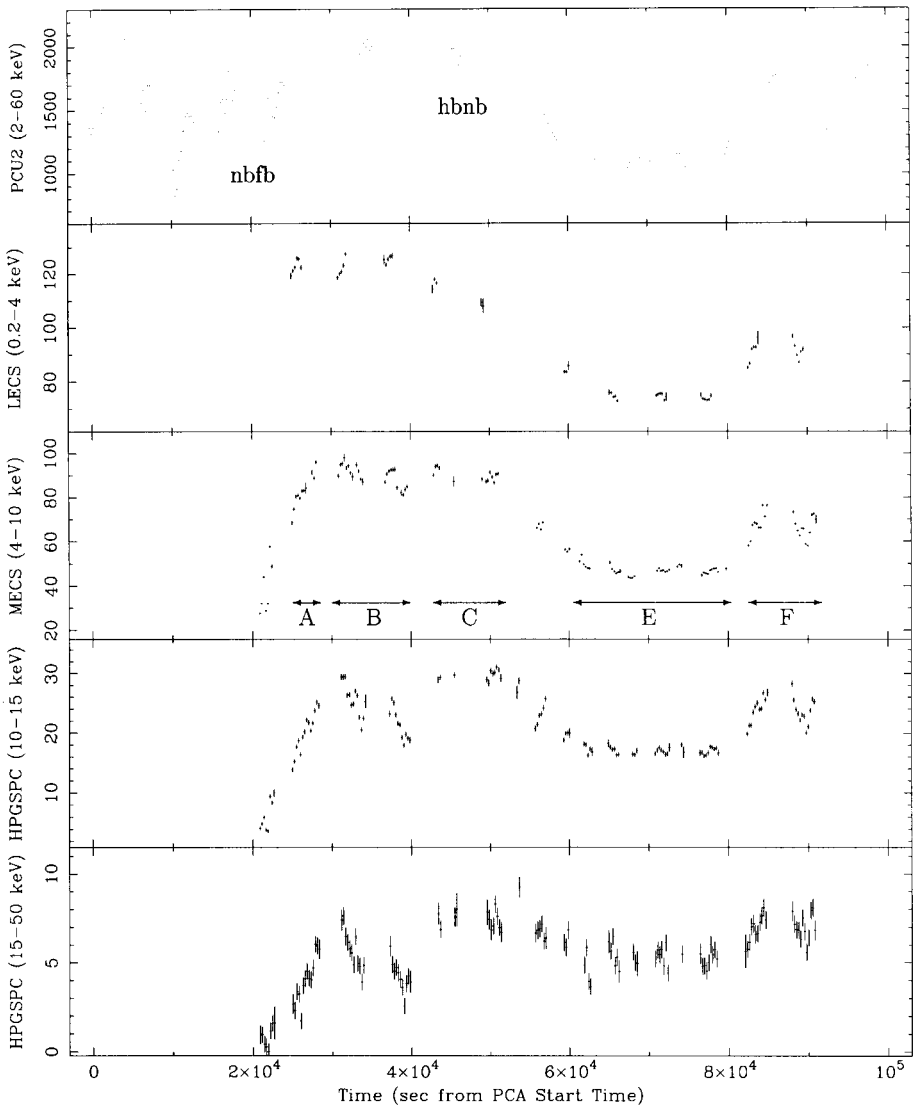

FIG. 2.—Light curves of Cyg X-2 in the energy range 2–60 keV of PCU2 (*top*) and in the four energy ranges 0.2–4, 4–10, 10–15, and 15–50 keV of the *BeppoSAX* NFIs. Each bin corresponds to 256 s. The PCA observation starts 20 ks before the *BeppoSAX* observation and ends 10 ks after.

BeppoSAX data were present. These spectra are denoted E, F, C, B, and A and reported in order of position along the Z track in Tables 3 and 4. The alphabetical order indicates the sequence in time (see MECS light curve in Fig. 2).

3. COLOR AND INTENSITY EVOLUTION

Figure 1 shows the *RXTE* ASM light curve of Cygnus X-2, where the long-term X-ray variation is clearly visible. The time of the *RXTE*/*BeppoSAX* observation is indicated with an arrow on the right. The light curve around the observation (see the inset in Fig. 1) shows complex time variability. The source was in the high overall intensity state (Kuulkers et al. 1996) and during the observation moved along the three branches of the Z pattern (this is more evident in the HID than in the CCD). No X-ray bursts occurred during the observation.

The *RXTE*/*BeppoSAX* light curves obtained in the entire energy range of the PCU2 and the various energy ranges of the NFIs are shown in Figure 2, and Figure 3 shows the color-color (CCD) and hardness-intensity (HID) diagrams. The bin size is 256 s. In Figure 3, each symbol indicates a different continuous segment in the light curve (see *top panel*).

The states of Z sources are typically described in terms of a horizontal branch (HB), a normal branch (NB), and a flaring branch (FB), as described above. The HB consists of the points with high hardness and varying intensity in the HID, the NB has high intensity and varying hardness, and the FB has low hardness and varying intensity. As observed during other high-intensity levels (Wijnands et al. 1997; Wijnands & van der Klis 2001), the FB in HID is almost horizontal, and the correlation of intensity with position along the Z track reverses in the FB relative to the HB. We divided the data into seven states for use in the analysis below. Four regions are in the HB (labeled hb1, hb2, hb3, and hb4 on the HID), one is in the NB (nb1), one region is at the NB/FB corner (nbfb), and finally one is in the FB (fb1).

The overall intensity of the source changed by more than a factor of 2 during the entire observation (see the PCU2 light curve). The character of the intensity variations changes with energy. Just after the beginning of the *BeppoSAX* observation, near a time of 2×10^4 s and

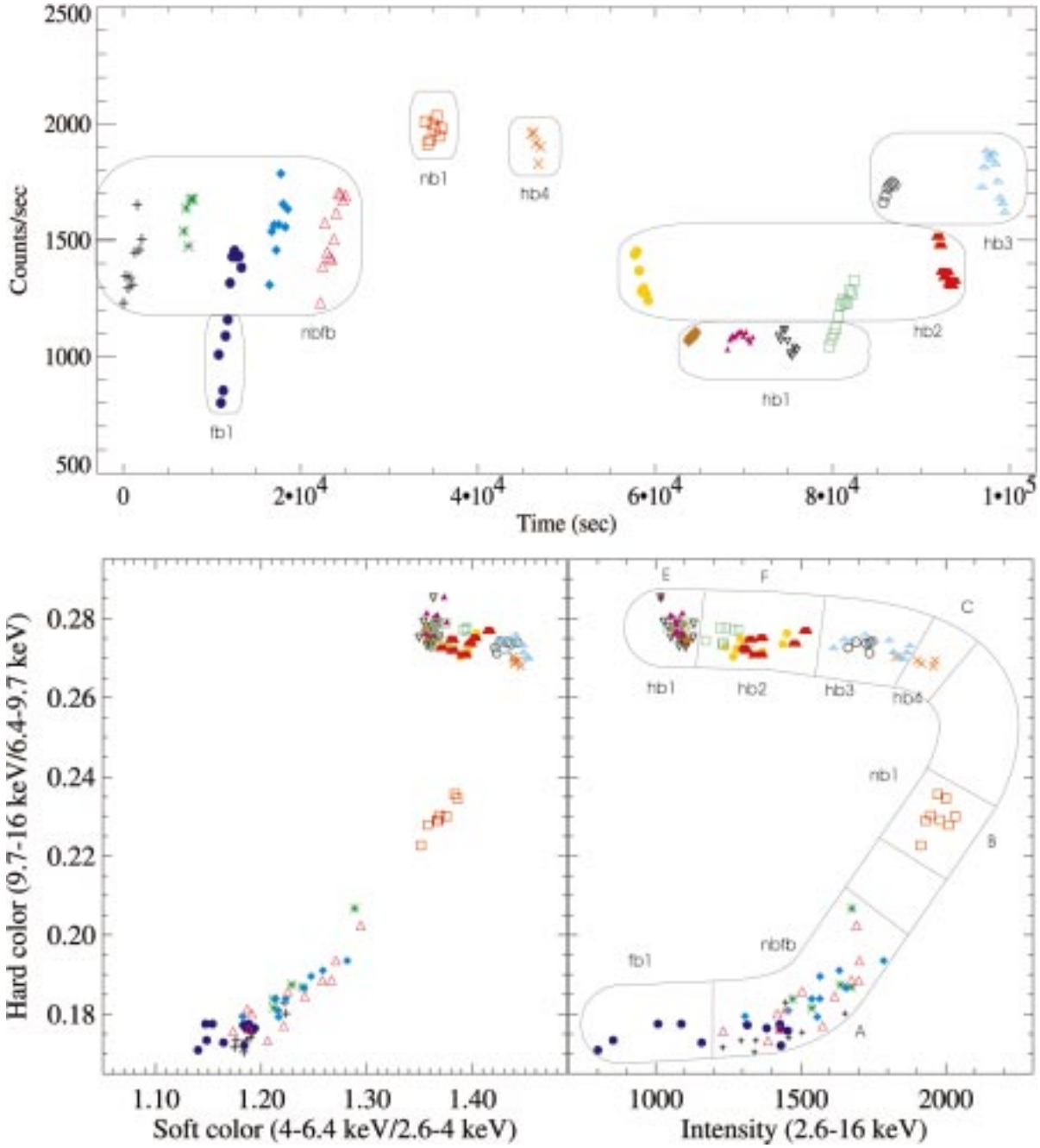

FIG. 3.—Light curve (*top*), CCD (*bottom left*), and HID (*bottom right*) of Cyg X-2. The soft color is the count rate ratio between 4.0–6.4 keV and 2.6–4.0 keV and the hard color that between 9.7–16 keV and 6.4–9.7 keV. Intensity was defined as the PCU2 count rates in the energy band 2.6–16 keV. All count rates were background-subtracted. All points are 256 s averages. Different colors and symbols were used for different continuous segments in the light curve, as shown in the top panel. Data regions used for the timing analysis are indicated in the HID diagram.

labeled nbfb in Figure 2, the source moved from the flaring branch (FB) to the normal branch (NB) and the count rates increased by more than a factor of 5 in the 4–10 keV, 10–15 keV, and 15–50 keV energy ranges but remained roughly constant in the 0.2–4 keV band. Conversely, near a time of 5×10^4 s and labeled hbnb in Figure 2, the source crossed the NB/HB corner, and the count rates in the bands below 10 keV decreased sharply, while the rate in the 15–50 keV band decreased only slightly.

4. FAST TIMING

To investigate the evolution of fast timing behavior with position in the HID, we created power spectra in the seven regions of the HID described above and shown in Figure 3. The resulting power spectra obtained from the full PCA band are shown in Figure 4, and power spectra obtained using events from the three higher energy single-bit channels, i.e., photons with energies above 5.8 keV, in Figure 5.

At least five different power spectral components have been distinguished in the power spectra of Cygnus X-2 and other Z sources (Hasinger & van der Klis 1989): (1) a power law referred to as very low frequency noise (VLFN) because it dominates below 0.1 Hz; (2) a broad noise component referred to as low-frequency noise (LFN), represented by a flat power law with a high-frequency cutoff, which characterizes the HB power spectra up to around 10 Hz; (3) a

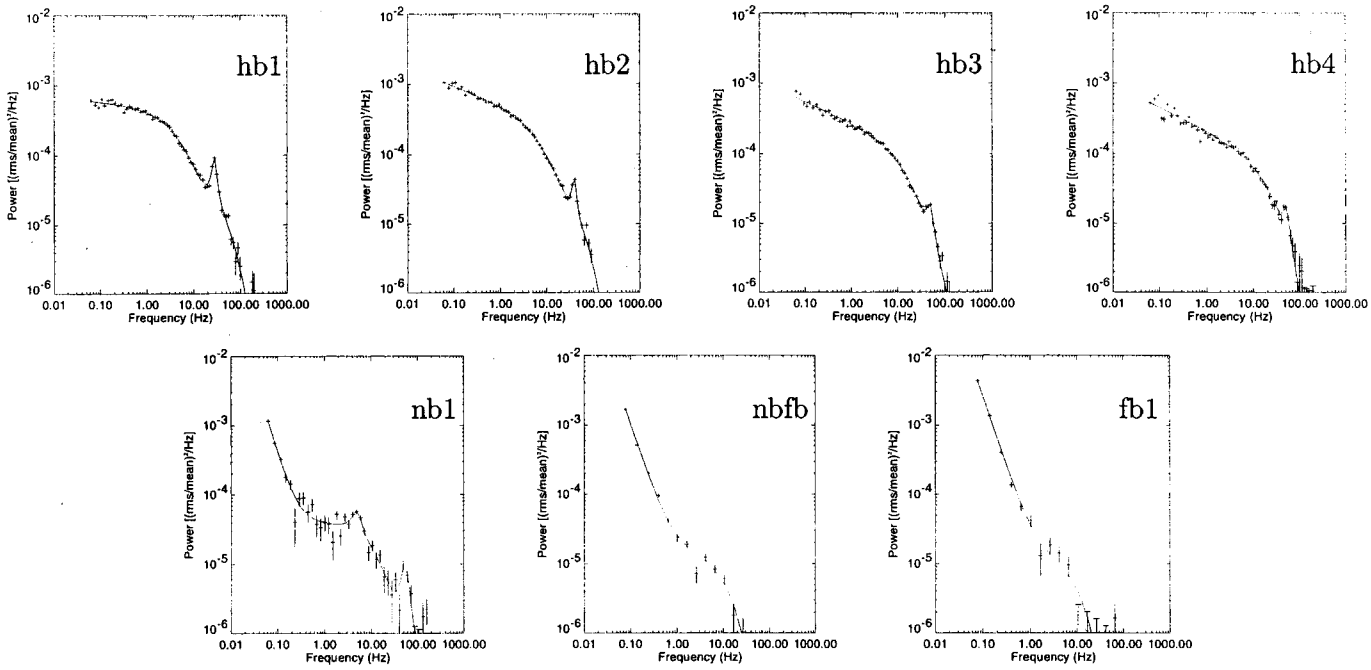

FIG. 4.—Power spectra obtained using data from all energy bands. The upper panels show spectra from the HB; the lower panels show the NB (*left*), the NB/FB (*middle*) and the FB (*right*) spectra, respectively.

broad noise component known as high-frequency noise (HFN), having a shape similar to LFN's, but extending to 100 Hz or above and present in all spectral states; (4) a narrow excess called the horizontal branch oscillation (HBO), with centroid frequency in the 15–60 Hz range, present in the HB and modeled with a Lorentzian; and (5) another broad peak, called the normal branch oscillation (NBO), present in the NB and similar in shape to the HBO, but with a characteristic frequency of around 6 Hz. The solid curves in Figures 5 and 6 represent analytic fits consisting of these components. The components used for each power spectrum and the fit parameters obtained are presented in Tables 1 and 2. The fractional rms amplitude for the VLFN component was found by integrating over the frequency range 0.001–1 Hz. A range of 0.01–100 Hz was used for both LFN and HFN components. Because the HFN power-law index α_H been found to be consistent with zero in Z sources (Hasinger & van der Klis 1989), we fixed it to zero.

A strong, narrow HBO is present at the left end of the HB (hb1). A faint and narrow feature was visible in the first three HB power spectra near the position of the second

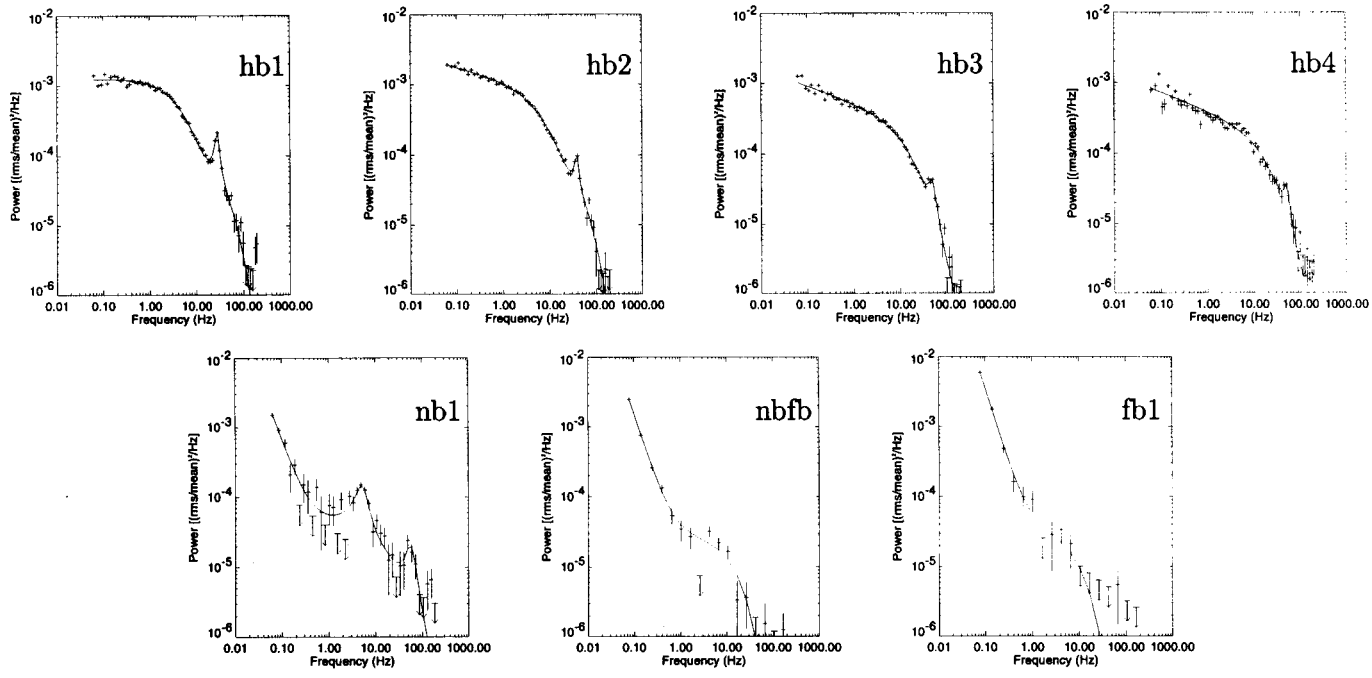

FIG. 5.—Same as Fig. 4, but for photons with energies above 5.8 keV

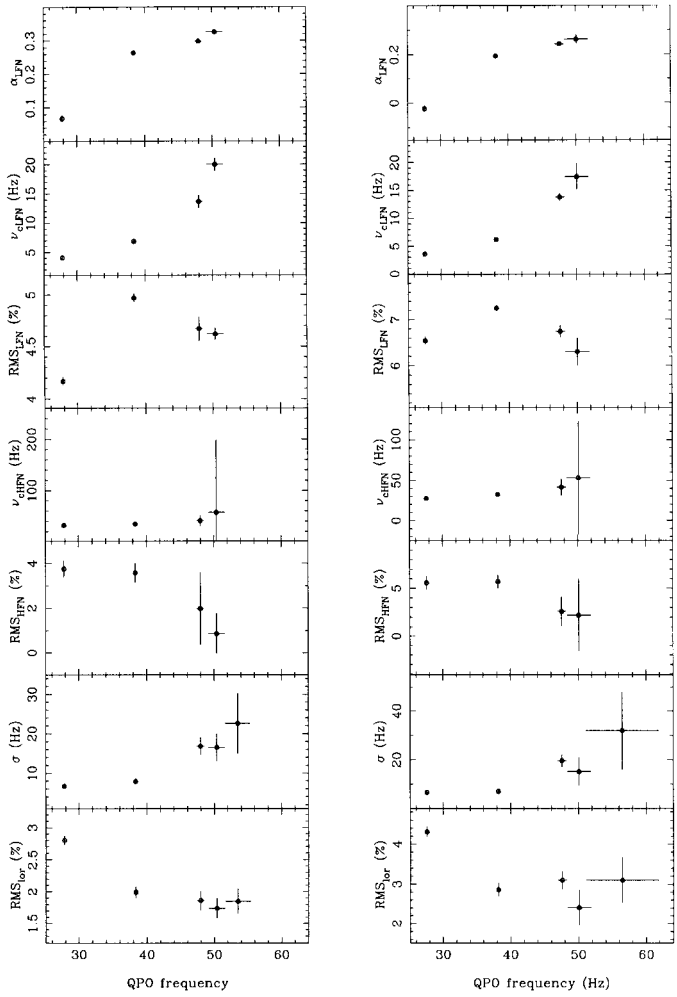

FIG. 6.—Best-fit parameters, obtained using the standard model for LFN and HFN, vs. HBO frequency. *Left*: values for power spectra extracted using all photons; *right*: power spectra extracted using photons with energies above 5.8 keV.

harmonic, and there is also a possible third harmonic in the hb1 power spectrum. Moving along the HB toward the NB, the frequency increased from 28 to 50 Hz, while its rms amplitude decreased from 2.8% to 1.7% (for $E > 5.8$ keV, the rms decreased from 4.3% to 2.4%) and its width increased from 6.7 to 16.5 Hz. This behavior is consistent with that observed in the *Ginga* data by Wijnands et al. (1997).

LFN and HFN can be identified in all four HB power spectra. The VLFN was not fitted separately from LFN because its power in the 0.1–100 Hz range was much smaller than that of LFN. The rms of the LFN was 4%–5% (6%–7% for $E > 5.8$ keV) and changed little along the HB. The power-law index α_{LFN} and the cutoff frequency $\nu_{c\,LFN}$ showed a positive correlation with the HBO frequency. The HFN component showed a cutoff frequency $\nu_{c\,LFN}$ consistent with remaining constant within the (sometimes large) errors and a clear inverse correlation between its strength and the HBO frequency.

On the upper part of the NB (nb1), the HBO was still visible at 54 Hz, with an rms level of 1.8% (3.1% for $E > 5.8$ keV). In addition, a broad NBO was present at ~ 5 Hz. The NBO feature was lost in the continuum as the source moved toward the FB. A very strong VLFN component (rms up to $\sim 17.4\%$) replaced the LFN in the continuum of the NB and FB power spectra. The VLFN became stronger moving from the NB to the FB, and the HFN showed the opposite trend.

5. SPECTRAL RESULTS

To investigate the spectral behavior versus the position on the Z track, we created energy spectra in the five regions of the HID described above. We fitted the X-ray continuum of Cyg X-2 with several two-component models. A blackbody or disk multicolor blackbody (DISKBB; Mitsuda et al. 1984) was used to model the soft component, and one of three thermal Comptonization models—a power law with cutoff, or the solution of the Kompaneets equation given by Sunyaev & Titarchuk (COMPST; 1980), or its improved version, in which relativistic effects are included (COMPTT; Titarchuk 1994)—was used for the harder component. The addition of a Gaussian around 1 keV was required in all intervals. Lines near 1 keV have been observed previously from Cyg X-2 with instruments with higher resolution (Vrtilek, Swank, & Kallman 1988). We also included a Gaussian near 6.7 keV to model possible Fe emission lines. The best fit to the continuum of Cyg X-2 was obtained using a blackbody or a DISKBB plus the COMPTT Comptonization model (hereafter BB + COMPTT and DISKBB + COMPTT, respectively).

Using the DISKBB + COMPTT model (Table 3; Fig. 7, *right panels*), adequate fits were obtained. There is a slight,

TABLE 1

RESULTS OF THE HB POWER SPECTRAL FITS OF THE PCA DATA

	LFN			HFN		HBO				
POWER SPECTRUM	α	ν (Hz)	rms (%)	ν (Hz)	rms (%)	ν (Hz)	Δν (Hz)	rms (%)	χ^2	DOF
hb1	0.068 ± 0.009	4.0 ± 0.2	4.17 ± 0.04	32 ± 2	3.8 ± 0.4	27.8 ± 0.1	6.7 ± 0.3	2.79 ± 0.07	270	65
hb2	0.264 ± 0.004	6.8 ± 0.3	4.97 ± 0.04	34 ± 3	3.6 ± 0.4	38.4 ± 0.2	7.8 ± 0.8	2.00 ± 0.09	330	65
hb3	0.299 ± 0.006	13.7 ± 1.1	4.67 ± 0.12	41 ± 10	2.0 ± 1.6	48.0 ± 0.5	16.8 ± 2.3	1.9 ± 0.1	470	65
hb4	0.326 ± 0.008	20.0 ± 1.1	4.62 ± 0.06	57 ± 141	0.9 ± 0.9	50.4 ± 1.3	16.5 ± 3.5	1.7 ± 0.2	222	65
$hb1_h$	−0.023 ± 0.012	3.6 ± 0.1	6.54 ± 0.08	28 ± 2	5.6 ± 0.7	27.6 ± 0.1	6.7 ± 0.4	4.3 ± 0.1	208	65
$hb2_h$	0.194 ± 0.007	6.2 ± 0.3	7.25 ± 0.07	33 ± 3	5.7 ± 0.7	38.2 ± 0.3	7.0 ± 1.1	2.9 ± 0.2	209	65
$hb3_h$	0.243 ± 0.007	13.8 ± 0.7	6.74 ± 0.13	41 ± 11	2.6 ± 1.5	47.6 ± 0.7	19.6 ± 2.7	3.1 ± 0.2	295	65
$hb4_h$	0.263 ± 0.018	17.4 ± 2.3	6.34 ± 0.30	53 ± 70	2.2 ± 4.0	50.1 ± 1.8	15 ± 6	2.4 ± 0.5	175	65

NOTES.—Power spectra hb1, hb2, hb3, and hb4 were extracted using data from all energy ranges; $hb1_h$, $hb2_h$, $hb3_h$, and $hb4_h$ were extracted using photons with energies above 5.8 keV.

TABLE 2

RESULTS OF THE NB AND FB POWER SPECTRAL FITS OF THE PCA DATA

	VLFN		HFN		HBO			NBO				
POWER SPECTRUM	α	rms (%)	ν (Hz)	rms (%)	ν (Hz)	$\Delta\nu$ (Hz)	rms (%)	ν (Hz)	$\Delta\nu$ (Hz)	rms (%)	χ^2	DOF
nb1	2.3 ± 0.1	10.5 ± 0.5	11 ± 2	2 ± 0.3	53.5 ± 1.9	23 ± 8	1.8 ± 0.2	5.0 ± 0.2	2.7 ± 0.8	1.2 ± 0.2	41	40
nbfb	1.98 ± 0.02	9.6 ± 0.1	8.9 ± 1.3	1.2 ± 0.1	...	...	...	...	...	...	32	17
fb1	2.04 ± 0.02	17.4 ± 0.1	7.6 ± 3.2	1.1 ± 0.4	...	...	...	...	...	...	34	17
$nb1_h$	1.92 ± 0.23	6.7 ± 0.7	18 ± 7	2.3 ± 1.9	56.5 ± 5.4	32 ± 16	3.1 ± 0.6	5.1 ± 0.2	3.5 ± 0.9	2.6 ± 0.4	34	40
$nbfb_h$.....	2.06 ± 0.06	13.4 ± 0.2	12.0 ± 2.9	1.9 ± 0.4	...	...	...	...	...	...	20	17
$fb1_h$	2.18 ± 0.07	25.6 ± 0.6	7.4 ± 5.0	1.7 ± 0.9	...	...	...	...	...	...	12	17

but not statistically significant, excess of counts at high energy in the E and F spectra. The parameters of the DISKBB component varied significantly with position along the Z track, with the inner disk temperature $kT_{\rm in}$ changing from 0.79 to 1.07 keV and the inner radius $r_{\rm in}$ changing from 34 to 25 km. Strong correlations of the parameters of the COMPTT component, other than its flux, with position along the Z track were not evident. The temperature and effective Wien radius of the seed photons for the Comptonized component were constant at $kT_{\rm W} \sim 1.2$ keV and $r_{\rm W} \sim 14$ km. The temperature of the Comptonizing region was also roughly constant at $kT_e \sim 3$ keV, while the optical depth varied in the range $\tau \sim 7$–10.

With the BB+COMPTT model, an excess of counts above $\sim$30 keV was apparent in all five spectra. Because it is now known that a hard tail is sometimes present in the spectra of Z sources, we added a power-law component to fit the hard tail. Addition of the power law is justified by the F-test statistic (the probability that the improvement in χ^2 is due to chance is always less than 3×10^{-5}). This additional component was detected up to energies of $\sim$80–100 keV, had a best-fit photon index $\sim$2.7, and contributed $\sim$14% of the 0.1–100 keV source flux.

Hard tails have been reported in the spectra of Z sources: e.g., for GX 5−1 using *Ginga* by (Asai et al. 1994), for Cyg X-2 using *BeppoSAX* (Frontera et al. 1999), for Sco X-1 using *CGRO*/OSSE (Strickman & Barret 2000) and using *RXTE*/HEXTE (D'Amico et al. 2001a), and for GX 17+2 (Di Salvo et al. 2000), GX 349+2 (Di Salvo et al. 2001), and Cir X-1 (Iaria et al. 2001) using *BeppoSAX* observations. The need for a hard power-law tail in the present data depends on the choice of the spectral model and thus

TABLE 3

RESULTS OF THE FIT OF CYG X-2 SPECTRA IN THE ENERGY BAND 0.2–80 KEV: DISKBB+COMPTT MODEL

	Spectrum and Z Region				
PARAMETER	E ⊂ hb1	F ⊂ hb2	C ⊂ hb4	B ⊂ nb1	A ⊂ nbfb
$N_{\rm H}(\times 10^{21}$ cm$^{-2})$	1.88 ± 0.05	1.96 ± 0.04	2.2 ± 0.1	2.0 ± 0.1	2.1 ± 0.1
$kT_{\rm in}$(keV)	0.79 ± 0.03	0.87 ± 0.01	1.02 ± 0.02	1.2 ± 0.3	1.07 ± 0.01
K[a].....	1016^{+150}_{-200}	800 ± 40	595^{+50}_{-80}	370^{+300}_{-190}	560 ± 30
$r_{\rm in}$(km)[b]	33.8 ± 3.7	30.0 ± 2.1	25.8 ± 2.2	20.4 ± 6.8	25.1 ± 1.8
$kT_{\rm W}$(keV)	1.15 ± 0.04	1.09 ± 0.02	1.26 ± 0.02	1.36 ± 0.1	1.25 ± 0.04
kT_e (keV)	3.3 ± 0.1	$2.95^{+0.05}_{-0.09}$	2.96 ± 0.10	3.3 ± 0.3	$3.1^{+0.8}_{-0.4}$
τ.....	8.2 ± 0.5	9.8 ± 0.3	8.9 ± 0.7	7.1 ± 0.9	7.0 ± 1.5
N_c.....	0.53 ± 0.05	$0.84^{+0.4}_{-0.2}$	1.01 ± 0.06	$0.7^{+0.3}_{-0.1}$	0.7 ± 0.15
y.....	1.74 ± 0.22	2.22 ± 0.15	1.83 ± 0.30	1.30 ± 0.35	1.19 ± 0.56
$r_{\rm W}$(km)[c]	13.2 ± 1.2	15.4 ± 0.7	13.9 ± 0.9	13.3 ± 2.9	15.3 ± 2.7
$E_{\rm line}$(keV)	1.08 ± 0.02	1.96 ± 0.04	1.06 ± 0.07	1.10 ± 0.04	1.03 ± 0.04
$\sigma_{\rm line}$ (keV)	0.09 ± 0.05	0.33 ± 0.07	$0.2^{+0.09}_{-0.05}$	0.13 ± 0.05	0.11 ± 0.05
$I_{\rm line}$(photons cm^{-2} s^{-1})	0.06 ± 0.04	$0.08^{+0.04}_{-0.06}$	$0.05^{+0.08}_{-0.05}$	0.44 ± 0.13	0.10 ± 0.04
Line EW (eV)	33	28	19	37	35
$E_{\rm Fe}$(keV)	6.8 ± 0.1	$6.4^{+0.1}_{-0.2}$	...	6.66 ± 0.16	$6.7^{+0.2}_{-0.5}$
$\sigma_{\rm Fe}$ (keV)	0.27 ± 0.1	1.13 ± 0.15	...	0.0[d]	0.0[d]
$I_{\rm Fe}$(photons cm^{-2} s^{-1}).....	$(4.0 \pm 0.8) \times 10^{-3}$	$(19 \pm 2) \times 10^{-3}$	...	$(1.3^{+4}_{-0.8}) \times 10^{-3}$	$(2.2^{+8.2}_{-1.2}) \times 10^{-3}$
Fe EW (eV)	48	140	...	8	17
$F_{\rm totab}(\times 10^{-8}$ ergs cm^{-2} s$^{-1})$...	1.53	2.00	2.60	2.62	2.29
$F_{\rm tot}(\times 10^{-8}$ ergs cm^{-2} s$^{-1})$	1.80	2.30	2.97	2.98	2.68
$L_{\rm tot}$ ($\times 10^{38}$ ergs s^{-1})	1.10	1.41	1.82	1.82	1.64
$\chi^2_{\rm red}$ (dof)	1.72 (112)	1.16 (118)	1.34 (116)	1.19 (112)	1.25 (114)

NOTES.—The model consists of a multicolor disk, COMPTT, and two Gaussian emission lines. For each spectrum the corresponding region in the PCA HID, as defined in Fig. 3, is indicated. Uncertainties are at the 90% confidence level for a single parameter. The total flux is in the 0.2–100 keV energy range.

[a] $K = (r_{\rm in}/D)^2 \cos i$, where $D = d/10$ kpc.

[b] Where $d = 7.2$ kpc and $i = 62.^{\circ}5$.

[c] Where $d = 7.2$ kpc.

[d] Value fixed during fitting.

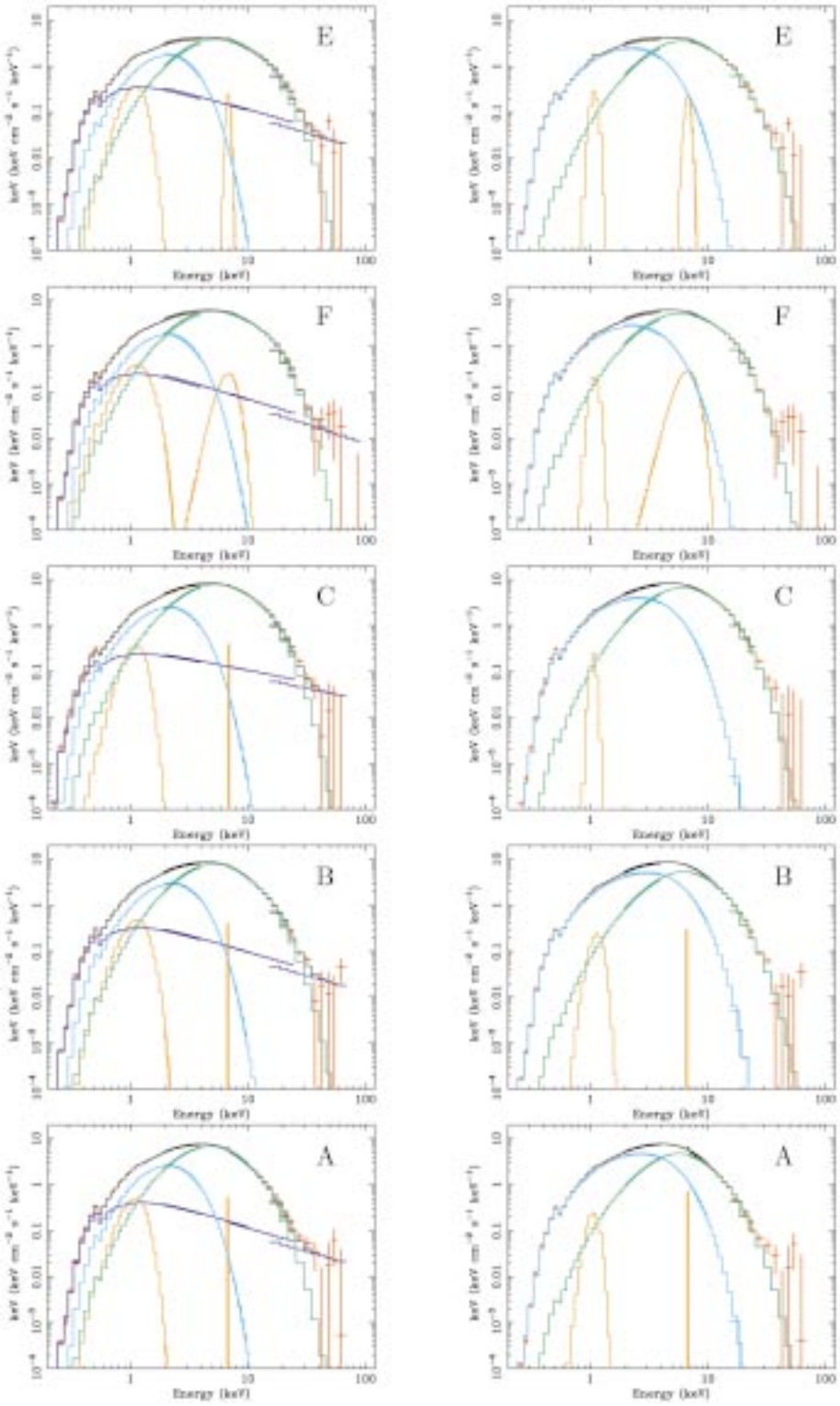

FIG. 7.—*Left*: Spectra (*red*) and best-fit models using BB + COMPTT + PO model. *Right*: Spectra and best-fit models using DISKBB + COMPTT. *Black line*: total model fit; *orange line*: emission lines; *light blue line*: disk model; *green line*: Comptonization component; *dark blue line*: power law.

cannot be considered a detection of the hard power-law tail. D'Amico et al. (2001b), taking into account all the results on the detections of hard X-ray tails in Sco X-1 and GX 349 + 2, argue that the appearance of such a component is correlated with the brightness of the thermal component. Specifically, they propose that the production of a hard X-ray tail in a Z source is a process triggered when the thermal component is brighter than $\sim 4 \times 10^{36}$ ergs s^{-1} in the 20–50 keV energy range. In this energy range, the luminosity of Cyg X-2, in the observation discussed here, was $\lesssim 2 \times 10^{36}$ ergs s^{-1}, i.e., very close to or slightly below the suggested trigger value. Hence, our results are apparently

consistent with previous observations. However, the fact that the hard power-law component is not required in the DISKBB+COMPTT model underscores the importance of understanding the low-energy emission in modeling the hard X-ray emission from X-ray binaries.

Results from these three-component fits to the *BeppoSAX* spectra of Cyg X-2 are given in Table 4 and in the plots on the left in Figure 7. Because the power-law normalization, absorption column N_H, and luminosity obtained by fitting the E-segment energy spectrum were surprisingly higher than those in other segments, we also report the fit parameters obtained by fixing the N_H-value to 2×10^{21} cm^{-2}, close to the average value from the other observations. The blackbody flux is well correlated with position along the Z track. The blackbody temperature and equivalent radius were approximately constant at $kT_{BB} \sim 0.5$ keV and $r_{BB} \sim 60$ km (using a distance of 7.2 kpc; Orosz & Kuulkers 1999), respectively. The temperature of the seed photons for the Comptonized component was roughly constant at $kT_W \sim 1$ keV. Following in 't Zand et al. (1999), we derived an effective Wien radius of the seed photons; this was roughly constant at $r_W \sim 20$ km. The temperature and optical depth of the (spherical) Comptonizing region were $kT_e \sim 3$ keV and $\tau \sim 9$, respectively.

The addition of an Fe K_α line at $\sim$6.7 keV proved necessary, especially when the source was in the HB (spectra E and F). Similar parameters for the line were found using both the BB+COMPTT and DISKBB+COMPTT models. *BeppoSAX* does not have adequate spectral resolution to draw detailed conclusions about the origin of this line (Piraino, Santangelo, & Kaaret 2000), but the presence of the line is motivation for high-resolution spectral studies of Cyg X-2 while in the HB.

6. CORRELATION OF SPECTRAL AND TIMING PARAMETERS

To directly compare the spectral and timing properties of Cyg X-2, we performed a second timing analysis of the *RXTE* data, using regions of the Z diagram matching the regions selected for spectral analysis. The analysis was performed as described above. In Figure 8, we plot the spectral parameters obtained for the Comptonization and thermal components of the E, F, C, and B spectra for the two models discussed above versus the HBO frequency. The flux from the Compton component seems correlated with HBO frequency for the BB+COMPTT model, but may not be for the DISKBB+COMPTT model. The other Comptonization parameters do not seem correlated with HBO frequency in either model. The total flux is clearly correlated with HBO frequency in both models. However, we

TABLE 4

RESULTS OF THE FIT OF CYG X-2 SPECTRA IN THE ENERGY BAND 0.2–80 KEV: BB+COMPTT MODEL

PARAMETER	Spectrum and Z Region					
	E ⊂ hb1	E (N_H fixed) ⊂ hb1	F ⊂ hb2	C ⊂ hb4	B ⊂ nb1	A ⊂ nbfb
N_H($\times 10^{21}$ cm^{-2})	3.9 ± 0.4	2.0 (fixed)	$1.9^{+0.9}_{-0.5}$	$1.5^{+2}_{-0.6}$	$1.9^{+1.7}_{-0.5}$	$2.2^{+1.7}_{-0.5}$
kT_{BB}(keV)	0.53 ± 0.02	0.50 ± 0.01	0.49 ± 0.03	0.52 ± 0.02	0.55 ± 0.02	0.51 ± 0.03
r_{BB}(km)	49.5 ± 3.7	59.9 ± 2.4	62.4 ± 7.7	62.9 ± 4.8	62.7 ± 4.6	68.4 ± 8.1
kT_W(keV)	1.06 ± 0.04	1.01 ± 0.03	0.94 ± 0.04	1.05 ± 0.05	1.08 ± 0.03	0.99 ± 0.04
kT_e (keV)	3.0 ± 0.2	3.0 ± 0.2	2.9 ± 0.1	2.7 ± 0.1	2.8 ± 0.2	$2.4^{+0.4}_{-0.2}$
τ	9.1 ± 0.6	9.3 ± 0.5	$9.8^{+0.3}_{-0.1}$	$9.9^{+0.8}_{-0.5}$	8.3 ± 0.7	$9.1^{+0.6}_{-1.3}$
N_c	0.64 ± 0.05	0.70 ± 0.05	$1.11^{+0.9}_{-0.5}$	1.53 ± 0.13	1.47 ± 0.15	1.62 ± 0.3
r_W(km)[a]	21.2 ± 2.1	16.9 ± 1.4	21.2 ± 2.0	18.9 ± 2.2	20.4 ± 1.9	23.2 ± 3.3
y	1.94 ± 0.29	2.03 ± 0.26	2.18 ± 0.12	2.07 ± 0.28	1.51 ± 0.28	1.56 ± 0.38
Photon Index α	3.2 ± 0.2	2.76 ± 0.1	$2.8^{+0.3}_{-0.2}$	2.5 ± 0.3	$2.7^{+0.3}_{-0.2}$	2.8 ± 0.3
Power-law N (photons keV^{-1} cm^{-2} s^{-1})[b]	2.4 ± 0.5	0.58 ± 0.6	$0.4^{+0.5}_{-0.2}$	$0.4^{+1.3}_{-0.3}$	$0.5^{+1.6}_{-0.2}$	$0.7^{+1.3}_{-0.4}$
E_{line}(keV)	1.06 ± 0.02	$0.97^{+0.05}_{-0.03}$	0.86 ± 0.16	$1.02^{+0.08}_{-0.12}$	$0.97^{+0.06}_{-0.09}$	$0.94^{+0.08}_{-0.06}$
σ_{line}(keV)	0.09 ± 0.05	0.23 ± 0.04	0.33 ± 0.07	$0.2^{+0.09}_{-0.05}$	$0.27^{+0.04}_{-0.14}$	0.24 ± 0.05
I_{line}(photons cm^{-2} s^{-1})	0.13 ± 0.04	0.34 ± 0.08	$0.6^{+0.4}_{-0.3}$	$0.23^{+0.25}_{-0.08}$	0.44 ± 0.13	0.5 ± 0.3
Line EW (eV)	44	176	242	115	186	181
E_{Fe}(keV)	6.80 ± 0.1	6.80 ± 0.1	$6.5^{+0.25}_{-0.3}$	6.7 ± 0.1	6.69[d]	6.74[d]
σ_{Fe}(keV)	0.25 ± 0.1	0.24 ± 0.14	$1.0^{+0.6}_{-0.3}$	0.0[d]	0.0[d]	0.0[d]
I_{Fe}(photons cm^{-2} s^{-1})	$(3.7 \pm 1) \times 10^{-3}$	$(3.6 \pm 1) \times 10^{-3}$	$(15 \pm 5) \times 10^{-3}$	0.0015[d]	0.0012[d]	0.0016[d]
Fe EW (eV)	44	44	115	10	8	13
F_{BB}($\times 10^{-8}$ ergs cm^{-2} s^{-1})	0.39 ± 0.03	0.45 ± 0.03	0.47 ± 0.04	0.60 ± 0.04	0.72 ± 0.3	0.63 ± 0.05
F_{totab}($\times 10^{-8}$ergs cm^{-2} s^{-1})	1.53	1.53	2.00	2.60	2.62	2.29
F_{tot}($\times 10^{-8}$ergs cm^{-2} s^{-1})	3.58	1.94	2.39	2.87	3.06	2.83
F_{BB}/F_{tot} (%)	11	23	20	21	23	22
L_{tot}[a] ($\times 10^{38}$ ergs s^{-1})	2.22	1.20	1.48	1.78	1.90	1.76
χ^2_{red} (dof)	1.68 (113)	1.80 (114)	1.19 (119)	1.18 (117)	1.09 (116)	1.00 (115)
F-test 1 (Fe)[c]	6.1×10^{-17}	5.4×10^{-13}	5.4×10^{-13}	2.3×10^{-2}	1.6×10^{-2}	8.3×10^{-3}
F-test 2 (power law)[c]	7.4×10^{-16}	5.1×10^{-15}	8.5×10^{-6}	2.7×10^{-5}	6.3×10^{-10}	1.1×10^{-14}

NOTES.—The model consists of blackbody, COMPTT, power law, and two Gaussian emission lines. For each spectrum the corresponding region in the PCA HID as defined in 3, is indicated. Uncertainties are at the 90% confidence level for a single parameter. The total flux is in the 0.2–200 keV energy range.

[a] Where $d = 7.2$ kpc.

[b] Power-law normalization at 1 keV.

[c] F-test 1 and F-test 2 are the probabilities of chance improvement when an iron line and power law are included in the spectral model.

[d] Value fixed during fitting.

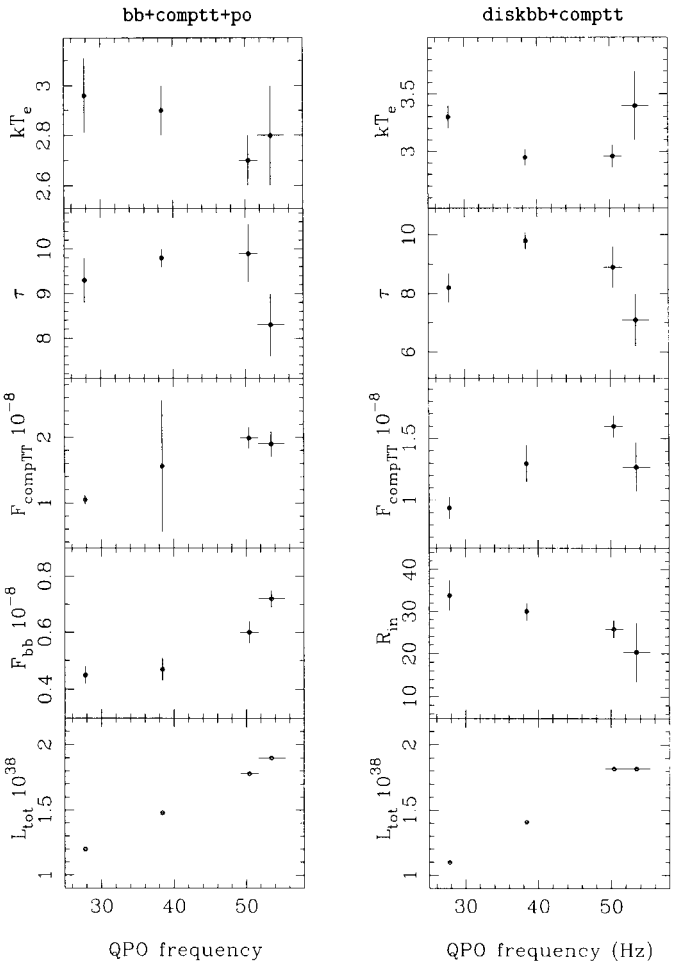

FIG. 8.—*Left*: Best-fit parameters from the energy spectrum analysis with BB+COMPTT+PO model vs. HBO frequency. *Right*: Same as *left panels*, but for spectrum analysis with DISKBB+COMPTT model.

note that these observations sample only a short time span, and correlations between timing parameters and total flux are generally not robust over long intervals (Ford et al. 1997). Interestingly, a strong correlation exists between the parameters of the soft spectral component, either the blackbody flux for the BB+COMPTT model or the disk inner radius for the DISKBB+COMPTT model, and the HBO frequency.

7. DISCUSSION

We discovered a correlation between the HBO frequency and the parameters of the soft thermal spectral component—the blackbody flux for the blackbody model and the disk inner radius for the multicolor disk blackbody model. This likely implies a physical relation between the source of the soft thermal emission and the timing frequencies.

RXTE and *BeppoSAX* data from the atoll source 4U 0614+091, covering a span of more than one year, showed a robust correlation between the kHz QPO frequency and the flux of the blackbody component in data spanning several years (Ford et al. 1997; Piraino et al. 1999). Because the frequencies of the various timing signals from X-ray binaries are highly correlated (Psaltis, Belloni, & van der Klis 1999), the physical implications of the spectral–HBO correlation are likely to be similar to those of the spectral–kHz QPO correlation.

A correlation would occur naturally in models where the oscillation frequencies are related to the Keplerian orbital frequency ν_K at inner edge of the accretion disk r_{in} (see, e.g., Alpar & Shaham 1985; Miller, Lamb, & Psaltis 1998; Stella & Vietri 1998) and the flux from the soft thermal component arises from an accretion disk (the usual interpretation of the DISKBB model). The Keplerian relation, $r_{in} \propto \nu_{HBO}^{-2/3}$, would be expected if the oscillation frequency ν_{HBO} is linearly related to the Keplerian orbital frequency ν_K. We fitted a function of the form $r_{in} = A\nu_{HBO}^{\alpha}$ to the data, with r_{in} taken as the disk radius from the DISKBB spectral component. The best-fit exponent is $\alpha = -0.5 \pm 0.2$, which is consistent with the Keplerian value $\alpha = -2/3$. With α fixed to the Keplerian value, the coefficient $A = 340 \pm 20$ km $\mathrm{Hz}^{2/3}$. This is consistent with a $\sim 2\ M_\odot$ neutron star if $\nu_{HBO}/\nu_K \sim 0.08$.

In the "magnetospheric beat-frequency model" (see, e.g., Alpar & Shaham 1985; Psaltis et al. 1999), the centroid frequency of the QPO is identified with the difference between the Keplerian frequency at magnetospheric radius and the spin frequency ν_S of the neutron star. If the inner disk radius is equal to the magnetospheric radius, then $r_{in} = (GM/4\pi^2)^{1/3}(\nu_{HBO} + \nu_S)^{-2/3}$. Fitting this form to the data, we find $\nu_S = 13 \pm 23$ Hz and $(GM/4\pi^2)^{1/3} = 410 \pm 120$ km $\mathrm{Hz}^{2/3}$. These values are inconsistent with a neutron star mass above 0.3 $M_\odot$. However, we note that r_{in} may not reflect the true magnetospheric radius.

The current data consist of only a few points, with significant errors in the derived spectral parameters for some of the points. Hence, the data are not sufficient to adequately constrain the relation between the oscillation frequency and the spectral parameters so that strong conclusions about the viability of particular models can be drawn. Additional observations, with higher spectral resolution and better low-energy response, made simultaneously with timing observations would be of great interest and might provide a means to discriminate among various models of the HBO.

We thank Evan Smith and Donatella Ricci for their efforts in coordinating the observations and the referee for important comments. P. K. and S. P. acknowledge support from NASA grants NAG 5-9104, NAG 5-9097, and NAG 5-7405.

REFERENCES

Alpar, M. A., & Shaham, J. 1985, Nature, 316, 239
Asai, K., Dotani, T., Mitsuda, K., Nagase, F., Kamado, Y., Kuulkers, E., & Breedon, L. M. 1994, PASJ, 46, 479
Boella, G., Butler, R. C., Perola, G. C., Piro, L., Scarsi, L., & Bleeker, J. A. M. 1997, A&AS, 122, 299
Bradt, H. V., Rothschild, R. E., & Swank, J. H. 1993, A&AS, 97, 355
Casares, J., Charles, P., & Kuulkers, E. 1998, ApJ, 493, L39
Cowley, A. P., Crampton, D., & Hutchings, J. B. 1979, ApJ, 231, 539
D'Amico, F., Heindl, W. A, Rothschild, R. E., & Gruber, D. E. 2001a, ApJ, 547, L147
———. 2001b, AIP Conf. Proc. 587, Gamma 2001, ed. S. Ritz, N. Gehrels, & C. R. Shrader (Melville, NY: AIP), 44
Di Salvo, T., Robba, N. R., Iaria, R., Stella, L. Burderi, L., & Israel, G. L. 2001, ApJ, 554, 49
Di Salvo, T., et al. 2000, ApJ, 544, L119
Ford, E. C., et al. 1997, ApJ, 486, L47

Frontera, F., et al. 1999, Nucl. Phys. B, 69, 286
Hasinger, G., & van der Klis, M. 1989, A&A, 225, 79
Hasinger, G., van der Klis, M., Ebisawa, K., Dotani, T., & Mitsuda, K. 1990, A&A, 235, 131
Iaria, R., Burderi, L., Di Salvo, T., La Barbera, A., & Robba, N. R. 2001, ApJ, 547, 412
in't Zand, J. J. M., et al. 1999, A&A, 345, 100
Kuulkers, E., van der Klis, M., & Vaughan, B. A. 1996, A&A, 311, 197
Miller, M. C., Lamb, F. K., & Psaltis, D. 1998, ApJ, 508, 791
Mitsuda, K., et al. 1984, PASJ, 36, 741
Orosz, J. A., & Kuulkers, E. 1999, MNRAS, 305, 1320
Piraino, S., Kaaret, P., Santangelo, A., & Ford, E. C. 1999, AAS HEAD meeting, 31, 15.24
Piraino, S., Santangelo, A., & Kaaret, P. 2000, A&A, 360, L35
Psaltis, D., Belloni, T., & van der Klis, M. 1999, ApJ, 520, 262
Stella, L., & Vietri, M. 1998, ApJ, 492, L59
Strickman, M., & Barret, D. 2000, in AIP Conf. Proc. 510, Fifth Compton Symposium, ed. M. L. McConnell & J. M. Ryan (Melville, NY: AIP), 222
Sunyaev, R. A., & Titarchuk, L. G. 1980, A&A, 86, 121
Titarchuk, L. 1994, ApJ, 434, 570
Vrtilek, S. D., Swank, J. H., & Kallman, T. R. 1988, ApJ, 326, 186
Wijnands, R., et al. 1998, ApJ, 493, L87
Wijnands, R., & van der Klis, M. 2001, MNRAS, 321, 537
Wijnands, R., van der Klis, M., Kuulkers, E., Asai, K., & Hasinger, G. 1997, A&A, 323, 399